

CHORUS. I. Cosmic HydrOgen Reionization Unveiled with Subaru: Overview

Akio K. INOUE^{1,2,3}, Satoshi YAMANAKA^{2,3}, Masami OUCHI^{4,5,6}, Ikuo IWATA^{4,7}, Kazuhiro SHIMASAKU^{8,9}, Yoshiaki TANIGUCHI^{10,11}, Tohru NAGAO¹¹, Nobunari KASHIKAWA⁸, Yoshiaki ONO⁵, Ken MAWATARI^{5,3}, Takatoshi SHIBUYA¹², Masao HAYASHI⁴, Hiroyuki IKEDA¹³, Haibin ZHANG^{14,5}, Yongming LIANG^{7,4,8}, C.-H. LEE¹⁵, Miftahul HILMI^{5,8}, Satoshi KIKUTA¹⁶, Haruka KUSAKABE¹⁷, Hisanori FURUSAWA^{4,7}, Tomoki HAYASHINO¹⁸, Masaru KAJISAWA¹¹, Yuichi MATSUDA^{4,7}, Kimihiko NAKAJIMA⁴, Rieko MOMOSE⁸, Yuichi HARIKANE^{19,4}, Tomoki SAITO²⁰, Tadayuki KODAMA²¹, Shotaro KIKUCHIHARA^{5,8}, Masanori IYE⁴ and Tomotsugu GOTO²²

¹Department of Physics, School of Advanced Science and Engineering, Faculty of Science and Engineering, Waseda University, 3-4-1, Okubo, Shinjuku, Tokyo 169-8555

²Waseda Research Institute for Science and Engineering, Faculty of Science and Engineering, Waseda University, 3-4-1, Okubo, Shinjuku, Tokyo 169-8555

³Department of Environmental Science and Technology, Faculty of Design Technology, Osaka Sangyo University, 3-1-1 Nakagaito, Daito, Osaka 574-8530

⁴National Astronomical Observatory of Japan, 2-21-1, Osawa, Mitaka, Tokyo, 181-8588

⁵Institute for Cosmic Ray Research, The University of Tokyo, 5-1-5 Kashiwa-no-ha, Kashiwa, Chiba 277-8582

⁶Kavli Institute for the Physics and Mathematics of the Universe (Kavli IPMU), WPI, The University of Tokyo, Kashiwa, Chiba 277-8583

⁷Department of Astronomical Science, The Graduate University for Advanced Studies, SOKENDAI, 2-21-1, Osawa, Mitaka, Tokyo 181-8588

⁸Department of Astronomy, Graduate School of Science, The University of Tokyo, 7-3-1 Hongo, Bunkyo-ku, Tokyo 113-0033

⁹Research Center for the Early Universe, Graduate School of Science, The University of Tokyo, 7-3-1 Hongo, Bunkyo-ku, Tokyo 113-0033

¹⁰The Open University of Japan, 2-11 Wakaba, Mihama-ku, Chiba, Chiba 261-8586

¹¹Research Center for Space and Cosmic Evolution, Ehime University, Matsuyama, Ehime 790-8577

¹²Kitami Institute of Technology, 165 Koen-cho, Kitami, Hokkaido 090-8507

¹³National Institute of Technology, Wakayama College, Gobo, Wakayama 644-0023

¹⁴Department of Astronomy, Tsinghua University, No.1 Qinghuayuan, Beijing 100084, China

¹⁵NSF's National Optical-Infrared Astronomy Research Laboratory, Tucson, AZ 85719, USA

¹⁶Center for Computational Sciences, University of Tsukuba, 1-1-1 Tennodai, Tsukuba, Ibaraki 305-8577

¹⁷Observatoire de Genève, Université de Genève, 51 chemin de Pégase, 1290 Versoix, Switzerland

¹⁸Research Center for Neutrino Science, Tohoku University, Aramaki, Aoba-ku, Sendai 980-8578

¹⁹Department of Physics and Astronomy, University College London, Gower Street, London WC1E 6BT, UK

²⁰Nishi-Harima Astronomical Observatory, Centre for Astronomy, University of Hyogo, 407-2 Nishigaichi, Sayo, Sayo-gun, Hyogo 679-5313

²¹Astronomical Institute, Tohoku University, 6-3 Aramaki, Aoba-ku, Sendai 980-8578

²²Institute of Astronomy, National Tsing Hua University, 101 Section 2 Kuang Fu Road, Hsinchu 300, Taiwan, R. O. C.

*E-mail: akinoue@aoni.waseda.jp

Received ; Accepted

Abstract

To determine the dominant sources for cosmic reionization, the evolution history of the global ionizing fraction, and the topology of the ionized regions, we have conducted a deep imaging survey using four narrow-band (NB) and one intermediate-band (IB) filters on the Subaru/Hyper Suprime-Cam (HSC), called Cosmic HydrOgen Reionization Unveiled with Subaru (CHORUS). The central wavelengths and full-widths-at-half-maximum of the CHORUS filters are, respectively, 386.2 nm and 5.5 nm for NB387, 526.0 nm and 7.9 nm for NB527, 717.1 nm and 11.1 nm for NB718, 946.2 nm and 33.0 nm for IB945, and 971.2 nm and 11.2 nm for NB973. This combination, including NB921 (921.5 nm and 13.5 nm) from the Subaru Strategic Program with HSC (HSC SSP), are carefully designed, as if they were playing a chorus, to observe multiple spectral features simultaneously, such as Lyman continuum, Ly α , C IV, and He II for $z = 2-7$. The observing field is the same as that of the deepest footprint of the HSC SSP in the COSMOS field and its effective area is about 1.6 deg². Here, we present an overview of the CHORUS project, which includes descriptions of the filter design philosophy, observations and data reduction, multiband photometric catalogs, assessments of the imaging quality, measurements of the number counts, and example use cases of the data. All the imaging data, photometric catalogs, masked pixel images, data of limiting magnitudes and point spread functions, results of completeness simulations, and source number counts are publicly available through the HSC SSP database.

Key words: catalogs — dark ages, reionization, first stars — galaxies: high-redshift — surveys

1 Introduction

Understanding cosmic reionization is one of the most important objectives in observational cosmology. Measurements of the Thomson scattering optical depth of free electrons in the intergalactic medium (IGM) in the cosmic microwave background with *Wilkinson Microwave Anisotropy Probe* and *Planck* satellites place the epoch of hydrogen reionization at $z \sim 10$ (Komatsu et al. 2011; Planck collaboration 2018). Detection of the Gunn-Peterson trough in the spectra of quasars at $z > 6$ (e.g., Fan et al. 2006; Becker et al. 2007) and the decrement in the luminosity functions (LFs) of Ly α emitters (LAEs) at $z > 6$ (e.g., Kashikawa et al. 2006; Ouchi et al. 2010; Hu et al. 2010; Kashikawa et al. 2011; Nakamura et al. 2011; Konno et al. 2014; Matthee et al. 2015; Santos et al. 2016; Konno et al. 2018; Itoh et al. 2018; Hu et al. 2019; Taylor et al. 2020) suggest a rapid increase in the hydrogen neutral fraction, x_{HI} , beyond $z = 6$. The x_{HI} measurements obtained so far still has a large scatter due to the small statistics and the systematic uncertainty in each measurement (e.g., Robertson et al. 2015; Greig &

Mesinger 2017; Inoue et al. 2018; Finkelstein et al. 2019; Naidu et al. 2020). New x_{HI} measurements near $z \sim 7$ based on large samples of galaxies over large cosmic volumes are required to reach a concordance in the history of reionization.

Galaxies, such as LAEs and Lyman break galaxies (LBGs), at $z > 6$ can be the dominant ionizing sources if their Lyman continuum (LyC) emissivity or escape fraction f_{esc} , is sufficiently high. The required f_{esc} is $\sim 20\%$, assuming a standard population synthesis model (e.g., Inoue et al. 2006; Robertson et al. 2015; Finkelstein et al. 2019; Naidu et al. 2020). Measuring the LyC emissivity of these galaxies, which is still quite uncertain, is the most critical step in the determination of the ionization sources for reionization. Bright quasars do not contribute much to the LyC emissivity for reionization owing to their rarity (e.g., Bianchi et al. 2001), whereas faint Active Galactic Nuclei (AGNs) might contribute to or even dominate (Giallongo et al. 2015; Madau & Haardt 2015). However, other observations suggest that faint AGNs are not sufficiently abundant (Kashikawa et al. 2015; Onoue et al. 2017; Matsuoka et

al. 2018; Parsa et al. 2018). Measuring the LyC emissivity of AGNs is also required to resolve their role in reionization (Micheva et al. 2017; Grazian et al. 2018). The metal-free stellar population, the so-called Population III (Pop III) stars (e.g., Carlberg 1981), can be an important ionizing source, particularly in the early phase of the reionization process (e.g., Sokasian et al. 2004). Because their characteristics, such as the initial mass function (IMF), are unknown observationally owing to the lack of information (Nagao et al. 2005; Nagao et al. 2008; Kashikawa et al. 2012; Vanzella et al. 2020), identifying Pop III clusters and revealing their nature are highly relevant to understanding their role in reionization.

Depending on the dominant ionizing source, the topology of reionization is expected to be different: “inside-out” (Iliev et al. 2006) by galaxies or “outside-in” (Miralda-Escudé et al. 2000) by X-ray sources, such as AGNs. Observationally, the spatial inhomogeneity of x_{HI} at $z \sim 6$ has been reported to be based on quasar spectra (Becker et al. 2015) and LAE LFs (Ouchi et al. 2010; Nakamura et al. 2011). Obtaining the overdensities of LAEs at $z \gtrsim 6.5$ may support the concept that these LAEs are located in the ionized bubbles produced by the galaxy overdensities (e.g., Castellano et al. 2016; Bagley et al. 2017; Higuchi et al. 2019; Harikane et al. 2019; Tilvi et al. 2020). Resolving the ionization topology is one of the main scientific goals for future H I 21 cm tomography with the Square Kilometer Array (SKA) (e.g., Hasegawa et al. 2016). However, with a sufficiently large survey of LAEs and LBGs, we may visualize the x_{HI} map before the SKA era. Such topology observations will be important consistency checks of the ionizing source observations, by comparing the observed topology with the prediction based on the identified dominant ionizing sources.

The Hyper Suprime-Cam (HSC) (Miyazaki et al. 2018; Komiyama et al. 2018; Kawanomoto et al. 2018; Furusawa et al. 2018) has the *widest* field-of-view (FoV), 1.75 deg², on an 8m-class telescope. This unique capability with a well-considered set of narrowband (NB) filters, for the first time, allows dealing with the central questions of reionization by an unprecedented wide and deep NB survey. Since 2007, we have studied the specifications of HSC NBs carefully (see section 2) and developed them under strict scientific reviews with the financial support of approximately 100 M yen from the Japan Society for the Promotion of Science. Four NBs (NB387, NB816, NB921, and NB101) among them are included in the on-going HSC Subaru Strategic Program (SSP) (Aihara et al. 2018a) for deep surveys of LAEs at $z \simeq 2.2, 5.7, 6.6,$ and 7.3 (Ouchi et al. 2018). The latter three high- z surveys provide new estimates of the cosmic average of x_{HI} at $z \simeq 6.6$ and 7.3 from comparison with LAE LFs (Ouchi et al. 2018; Shibuya et al. 2018a; Shibuya et al. 2018b; Konno et al. 2018; Inoue et al. 2018). However, the HSC SSP cannot address the LyC emissivity and the x_{HI} topology directly.

Thus, we initiated a Subaru intensive program, Cosmic HydrOgen Reionization Unveiled with Subaru (CHORUS), with NB387, NB527, NB718, IB945, and NB973 (Table 1; see Fig. 1). Supplying the data of the NB921 and broadband (BB) filters from the HSC SSP, we aim to answer the questions of the ionization source and the topology, in addition to the history, by measuring the LyC emissivity values of galaxies and AGNs, abundance of Pop III stars, and LF of faint AGNs, and visualizing the x_{HI} map directly (see sections 6.1-6.5 for more information). These measurements are realized only in combination with our NBs. This program will become a legacy survey at least for a decade because no other deep and wide-area survey, such as the Large Synoptic Survey Telescope, has a set of NBs like this program.

This paper presents an overview of the CHORUS project and its first public data release: CHORUS PDR1. In section 2, we describe the CHORUS filter set in detail. Section 3 is a summary of the observations, data reduction, and photometric catalogs of the CHORUS data. Section 4 presents a summary of imaging quality, such as the size of the point spread function and the limiting magnitude of each NB. In section 5, the number counts in the five CHORUS NBs are given as a set of fundamental measurements of the NB imaging data. Section 6 gives a brief instruction of the usage of the CHORUS PDR1 data and some example science cases. A summary of this paper is found in the final section.

We assume a standard set of cosmological parameters of $H_0 = 70 \text{ km s}^{-1} \text{ Mpc}^{-1}$, $\Omega_M = 0.3$ and $\Omega_\Lambda = 0.7$ and use the AB magnitude system (Oke 1990) throughout the study.

2 Filter set

The CHORUS filter set consists of four NBs (NB387, NB527, NB718, and NB973) and one IB (IB945) in addition to NB921 from HSC SSP. Table 1 is a summary of the characteristics of the filters and the targeted spectral features of high- z galaxies and the redshift ranges. Fig. 1 shows the total efficiency of the NBs as well as HSC BBs.¹ The CHORUS filter set not only covers a wide redshift range of $2 \lesssim z \lesssim 7$ of Ly α but also enables us to observe multiple spectral features at specific redshifts at the same time. As found in Fig. 1, the LyC and He II 1640 line for $z \simeq 3.3$ LAEs selected with NB527 can be observed with NB387 and NB718, respectively, and similarly, the LyC, C IV line, and He II line for $z \simeq 4.9$ LAEs selected with NB718 can be observed with NB527, NB921, and NB973, respectively.

¹ In the UD COSMOS field of the HSC SSP, there are two filters each for the r - and i -bands, namely $r2/r$ and $i2/i$ (Kawanomoto et al. 2018). The newer $r2$ and $i2$ filters were used about 60% in the data according to the HSC PDR2 web page (<https://hsc-release.mtk.nao.ac.jp/doc/index.php/data-2/>). These two filter images were all combined to make final coadd images of the r - and i -bands (Aihara et al. 2019).

Table 1. Summary of filter properties.

Filter	Area-weighted mean (Central position)			Redshift range of targeted features ^d				Papers which used the NBs. ^e
	CW ^a	FWHM ^b	TP ^c	LyC	Ly α	C IV	He II	
NB387	386.2 (385.8)	5.5 (5.7)	0.842 (0.871)	>3.27	2.15–2.20	—	—	A18a, L20
NB527	526.0 (525.5)	7.9 (7.5)	0.956 (0.922)	>4.81	3.29–3.36	—	2.18–2.23	H20
NB718	717.1 (716.8)	11.1 (11.1)	0.927 (0.911)	—	4.85–4.94	—	3.34–3.41	Z20, H20
NB921 ^f	921.5 (920.4)	13.5 (13.4)	0.935 (0.937)	—	6.52–6.64	4.90–4.99	—	A18a, O18, H20
IB945	946.2 (944.7)	33.0 (32.2)	0.955 (0.952)	—	6.65–6.92	—	—	
NB973	971.2 (969.9)	11.2 (11.0)	0.878 (0.834)	—	6.94–7.04	—	4.88–4.95	I18, H20

^a The central wavelength (CW) of the transmission function in units of nm.

^b The full-width-at-half-maximum (FWHM) of the transmission function in units of nm.

^c The transmission peak (TP) of the transmission function itself (i.e., not including the instrumental and atmospheric throughput).

^d $(CW \pm FWHM/2)/\lambda - 1$. Adopted rest-frame wavelength (λ) of the features: Lyman limit: 91.175 nm, Ly α : 121.567 nm, C IV: 154.949 nm, and He II: 164.033 nm.

^e References: A18a: Aihara et al. (2018a), L20: Liang et al. (2020), H20: Hayashi et al. (2020), Z20: Zhang et al. (2020), O18: Ouchi et al. (2018), I18: Itoh et al. (2018)

^f The imaging data collected and presented in SILVERRUSH (Ouchi et al. 2018) of the HSC SSP (Aihara et al. 2018a).

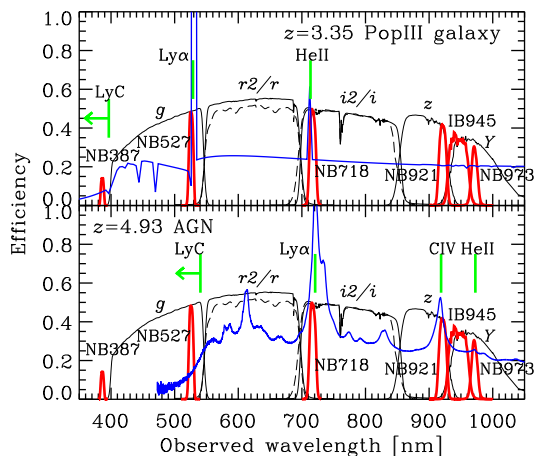


Fig. 1. Filter efficiency functions (narrowbands and broadbands are shown in red and black, respectively) with example spectra of a galaxy at $z = 3.35$ (top) and an AGN at $z = 4.93$ (bottom). For the $r2/r$ and $i2/i$ bands, the solid lines show the $r2$ and $i2$ transmissions and the dashed lines show the r and i transmissions. The effects considered in addition to the filter transmission are as follows: atmospheric transmission at the summit of Mauna Kea (airmass of 1.2 and water vapor column of 1.6 mm), the primary mirror reflectance, and the instrumental throughput of the HSC including the CCD quantum efficiency and an average vignetting effect in the field-of-view.

For $z \simeq 2.2$ LAEs selected with NB387, the He II line can be observed with NB527 (see Table 1). The last CHORUS filter, IB945, is a filter to select LBGs within a redshift range similar to that of LAEs selected with NB921 ($z \simeq 6.6$) and NB973 ($z \simeq 7.0$) (see section 6.4 for its science case). It is also useful to trace the line-free continuum between the C IV and He II lines at $z \simeq 4.9$ (see Fig. 1). In the following, we further describe the philosophy of the HSC SSP and CHORUS filter specifications and the characteristics of the CHORUS filters measured in the laboratory.

The NB filter set for the HSC imaging survey was designed very carefully (Ouchi et al. 2018). The filter wavelengths in the redder wavelength range were determined to pass through OH sky windows at 816, 921, 973, and 1010 nm. The three filters,

except for the one at 973 nm, were used for the NB imaging observations in the HSC SSP survey (Aihara et al. 2018a) called SILVERRUSH (Ouchi et al. 2018). The remaining NB973 filter became a CHORUS filter. The filter wavelengths in the blue wavelength range were determined to ensure that multiple spectral features of the LAEs selected by an NB filter were captured by the other NB filters and strong rest-frame optical emission lines of the LAEs passed through the OH sky windows in the near-infrared range maximally. The selected wavelengths were 387, 527, and 718 nm, which became the CHORUS filters.² This combination allows us to observe LyC, Ly α , and He II at $2 \lesssim z \lesssim 5$ as described above. The [O II] 3727 and H α lines for $z \simeq 2.2$ LAEs selected with NB387 fall in the OH sky windows at 1.19 and 2.10 μm . The [O III] 4959/5007 for $z \simeq 3.3$ LAEs selected with NB527 are also observable at 2.15/2.17 μm in the middle of the K -band.

The full-width-at-half-maximum (FWHM) of each filter was also determined carefully (Ouchi et al. 2018). The FWHM of NB921 was first determined, to cover the full width of the OH sky window. The FWHMs of the other NB filters, except for NB973 and IB945, were subsequently determined to ensure the same efficiency for the Ly α line detection as NB921. Because the observed equivalent width of a line is $EW_{\text{obs}} = (1+z)EW_0$, where EW_0 is the intrinsic equivalent width and z is the source redshift, the FWHMs were determined by the relation, $FWHM = FWHM_{921} \times (1+z)/(1+6.58)$. Note that 6.58 is the redshift of the LAEs selected with NB921. NB973 has a narrower FWHM than the relation to enhance the efficiency of the Ly α line detection and compensate for the shallower depth in the band. IB945 has an FWHM to fill the wavelength gap between NB921 and NB973.

The HSC filter is 600 mm in diameter, making it a challenging task to realize a uniform multi-layer interferometric coating

² Although NB387 was also used for the ‘Deep’ layer observations in the HSC SSP (Aihara et al. 2018a; Ouchi et al. 2018), there was no data taken in the footprint of the ‘UltraDeep’ layer in the COSMOS field, where the CHORUS observations were performed.

to produce narrow bandpass filters with sharp cut-on and cut-off wavelengths. Therefore, there was a small deviation from the specifications during the production process. We examined the performance of the NB filters produced by the manufacturers, Optical Coatings Japan (NB387, NB527, NB718, NB921, and NB973) and Materion (IB945), using the method described in Kawanomoto et al. (2018). Slight non uniformities in the central wavelength (CW), FWHM, and transmission peak (TP) were found along the radial direction. The CW tended to increase with the radius, except for NB387 where the CW variation was a complex way. The FWHM also tended to increase in the outer part, except for NB387 where it decreased with the radius. The overall CW variation was less than 0.3–0.5% (the worst case was found in NB527), whereas the FWHM variation is ranging from a few–10% (NB387). The TP also tended to increase with the radius, except for NB387 again, where the TP decreased with the radius. The overall TP variation was less than 1–10% (NB973). A higher degree of uniformity was found in the azimuthal direction. Table 1 presents the CWs, FWHMs, and TPs for the area-weighted mean transmission functions of the CHORUS filters. The values for the transmission functions at the center positions of the filters are also provided for reference. The machine-readable filter transmission curves are available at the Subaru/HSC web site.³

3 Observations, data reduction and photometric catalogs

We were awarded 13 nights in the classical mode of the Subaru Telescope for four consecutive semesters from S16B to S18A (i.e., 2 years) under a Subaru open-use intensive program, S16B-001I (PI: A. K. Inoue). We were also awarded 11.5 hours in the queue mode in semester S18B under an open-use normal program, S18B-004 (PI: A. K. Inoue), to supplement the time loss due to the weather during the original four semesters. Under the two programs, we performed deep imaging observations using our NB filters on the HSC on the dates listed in Table 2. The on-source exposure time as well as the effective exposure time used for the final coadd images are also listed in Table 2. Some of the observation dates were not under a photometric condition (i.e., low transparency), and we discarded a fraction of the observed data owing to bad quality. The observing field was the COSMOS field (Scoville et al. 2007), which has the same footprint as the HSC SSP Ultra Deep (UD) layer (Aihara et al. 2018a). Any sky region in the HSC SSP survey is defined by a set of two numbers of `tract` and `patch` (Aihara et al. 2018b). Most of the HSC SSP UD COSMOS is covered by `tract` number 9813. There are 9×9 sub-regions — `patches` — in a `tract`. Each `patch` has a sky area of $12' \times 12'$ and a `tract` has that of $1.8^\circ \times 1.8^\circ$. The numbers of `patches` are expressed

as 000 (south-east corner), 001, 002, ..., 008 (north-east corner), 100, 101, ..., 808 (north-west corner). The `patch` configuration in the UD COSMOS `tract` 9813 is found in Fig. 2.

The data reduction was conducted using the HSC SSP pipeline, `hscPipe`, version 6.7, which is the same as that used for the SSP PDR2 data processing. We used the obtained imaging data satisfying the following conditions: exposure time = 1200 sec, seeing $< 1.5''$, and transparency > 0.4 for NB387, exposure time = 1200 sec (but 3 frames of 468–1016 sec), seeing $< 1.2''$, and transparency > 0.75 for NB527, exposure time = 1200 sec, seeing $< 1.2''$, and transparency > 0.76 for NB718, exposure time = 1200 sec, seeing $< 1.2''$, and transparency > 0.9 for NB973, and exposure time = 720 sec, seeing $< 1.2''$, and transparency > 0.7 for IB945. `hscPipe` generates several multiband photometric catalogs, which we call “CHORUS PDR1 catalog.” The source detection is based on the signal-to-noise ratio (S/N) within the PSF against the background noise fluctuation (Bosch et al. 2018) and the detection criterion is 5σ , the same as the SSP PDR papers (Aihara et al. 2018b; Aihara et al. 2019). The readers should refer to pipeline paper (Bosch et al. 2018) and the SSP PDR2 paper (Aihara et al. 2019) for the detailed procedures of the data reduction, source detection, and photometry. In the following, we describe some specific points for the CHORUS data release.

The photometric zero-points for the CHORUS NBs were determined based on the BB photometry of the Galactic stars in the Pan-STARRS1 (PS1) catalog (Chambers et al. 2016) similar to the method for the HSC SSP (Aihara et al. 2018b; Aihara et al. 2019). The color terms translating PS1 BB magnitudes to HSC NB magnitudes were estimated based on the Pickles stellar spectral templates (Pickles 1998). This seems work well, except for NB387, where a systematic zero-point offset was found in Liang et al. (2020) (and see the last paragraph in this section). The multiband photometry was conducted with the so-called *priority order* (Bosch et al. 2018) of the filters, which was defined as i, r, z, y, g for the BB filters, followed by the order of NB921, NB816, NB973, NB718, NB527, NB1010, NB387, and IB945 for the NB filters. The priority order of the filters was used to determine the object positions.⁴ For the line emitters detected in a single NB image but not detected in any other BB and NB images, photometry on the NB image was conducted at the positions of the detections in the NB image. However, for the line emitters that were also detected in other BB (and NB) images, the photometry positions were forced to be the positions in the most prioritized band among the images in which the objects were detected. In such cases, photometry

⁴ This is the so-called *forced* catalog based on multiband photometry at the positions in the most prioritized band. The `hscPipe` makes another catalog based on photometry at the positions in each band separately, called *meas* (or *unforced*) catalog (Aihara et al. 2018b). We do not deal with the *meas* catalog in this paper because the photometry may not give reliable colors owing to potentially different positions in different bands.

³ <https://subarutelescope.org/Observing/Instruments/HSC/sensitivity.html>

Table 2. Summary of CHORUS observations and data qualities.

Filter	Observation dates	Exposure ^a	PSF FWHM ^b	5 σ depth ^c [AB]		Area ^d
		[h]	[$''$]	$\phi 1.5''$	$\phi 2.0''$	[deg ²]
NB387	Jan. 17, 18, 19, 2018	21/17.3	1.01 (0.99)	25.80 ^e (26.07) ^e	25.42 ^e (25.65) ^e	1.561
NB527	Dec. 16, 17, 18, 2017; Mar. 15, 16, 18, 2018	10.5/8.9	0.83 (0.82)	26.72 (26.87)	26.30 (26.46)	1.613
NB718	Feb. 25, Mar. 23, 25, 2017	13.5/7.7	0.69 (0.68)	26.29 (26.47)	25.87 (26.06)	1.575
IB945	Dec. 1, 2, 3, 12, 2018	10.2/10.2	0.62 (0.61)	25.77 (25.92)	25.36 (25.49)	1.558
NB973	Jan. 26, 28, 2017	15/14.7	0.64 (0.64)	25.19 (25.37)	24.79 (24.96)	1.603

^a On-source exposure time/effective exposure time for the final coadd image, except for patches at the edge of the field-of-view, where these times are somewhat shorter due to dithering.

^b Full-width-at-half-maximum (FWHM) of the point spread function (PSF): The area-weighted average value (the value in the central patch 404).

^c 5 σ limiting magnitude for circular apertures of 1.5 $''$ or 2.0 $''$ in diameter: The area-weighted average value (the value in the central patch 404).

^d Effective area after removing masked regions.

^e Value corrected for zero-point offset (-0.45 mag.). See an explanation in the last paragraph of section 3.

on the NB image, which includes the line flux, can be underestimated if there are spatial offsets between the prioritized band and NB positions. This would not be a problem for the bright objects that are detected well both in the prioritized band and NB images; however, it might be an issue for the objects that are marginally detected in the prioritized band and whose positions in the band have a large uncertainty. Quantifying this effect would need a large set of pipeline simulations that was reserved for future line emitter analyses.

There are several different photometric magnitudes in the CHORUS PDR1 multiband catalog. In this paper, we do not recommend using `cmode1` magnitudes, which represent the total flux densities obtained by the brightness profile fitting (Bosch et al. 2018) and were considered representative magnitudes in SSP PDR1 (Aihara et al. 2018b). This is because there is an issue of erroneously bright `cmode1` magnitudes for some objects in SSP PDR2 (Aihara et al. 2019) and a follow-up study (Hayashi et al. 2020). According to section 6.6.3 of the SSP PDR2 paper (Aihara et al. 2019), this problem is likely to be caused by a failure in the deblending procedure in crowded regions of objects. This problem can be severe in the HSC SSP UD footprint in the COSMOS field, where the CHORUS observations were performed, because the very deep BB depth yields a very high density of the detected objects.

We instead recommend using the `undeblended_convolvedflux` magnitudes for estimates of total magnitudes.⁵ These measurements are based on the aperture magnitudes of the final coadd images smoothed with a Gaussian function (see section 3.6 of the SSP PDR1 paper, Aihara et al. 2018b). The Gaussian smoothing size is defined as the resultant FWHM of the point sources in the smoothed images, which is 0.59 $''$, 0.84 $''$, 1.1 $''$, or 1.3 $''$ (Aihara et al. 2019). This process produces a set of the smoothed BB and

NB images with the selected same PSF FWHM. Subsequently, the flux densities of each object in all the smoothed (i.e., PSF-matched) images are measured in a circular aperture of diameter size 1.1 $''$, 1.5 $''$, 2.0 $''$, or Kron-size, and aperture corrections are also applied assuming a point-source.⁶ This process is performed for all the detected objects as a function of `hscPipe` (Aihara et al. 2018b; Aihara et al. 2019). These PSF-matched magnitudes yield better colors in crowded fields (Aihara et al. 2018b), which is the most important feature to reliably select LAEs in two-color diagrams. This procedure is very similar to the method performed in previous studies with `SExtractor` (Bertin & Arnouts 1996). In this study, we adopt 1.5 $''$ (2.0 $''$)-diameter apertures on 0.84 $''$ (1.1 $''$)-smoothed images.⁷

There are two significant known issues in the SSP PDR2 photometric catalog (Aihara et al. 2019), and they are prevalent in the CHORUS PDR1 catalog also produced by `hscPipe` 6.7. The first one is that the uncertainties of the PSF-matched magnitudes are underestimated (section 5.8.11 of the SSP PDR1 paper, Aihara et al. 2018b). This occurs because covariances are introduced by the Gaussian smoothing process. This problem persists in the SSP PDR2 release (Aihara et al. 2019). Therefore, we do not recommend using these cataloged values of uncertainties for the PSF-matched magnitudes. Instead, we estimated the uncertainties by measuring the rms values of the aperture flux densities in the actual images. The limiting magnitudes provided in the next section are based on these measurements.⁸ The second issue is that there is a systematic offset

⁶ The amount of the aperture correction can be found as `undeblended_convolvedflux_X.Y_apcorr` in the catalog database, where X and Y are the numbers indicating the target convolution size and the aperture size, respectively.

⁷ If the native PSF of a band is larger than the target smoothing FWHM, any Gaussian smoothing is not applied to the band and simply the native images are used for the aperture photometry (see section 3.6 of Aihara et al. 2018b). Such a case happened for NB387 in the 0.84 $''$ target FWHM smoothing.

⁸ The uncertainty in a magnitude is given by $\delta m = (2.5/\ln 10)/(S/N)$. The signal-to-noise ratio, S/N , of each object can be estimated from the ratio of `undeblended_apertureflux` in the catalog database to the 1 σ aperture

⁵ There is another similar measurement called `convolvedflux`, for which the source deblender algorithm in `hscPipe` works. On the other hand, the source deblending process was turned off for `undeblended_convolvedflux`. We have found that the two magnitudes of `undeblended_convolvedflux` and `convolvedflux` are identical in most cases.

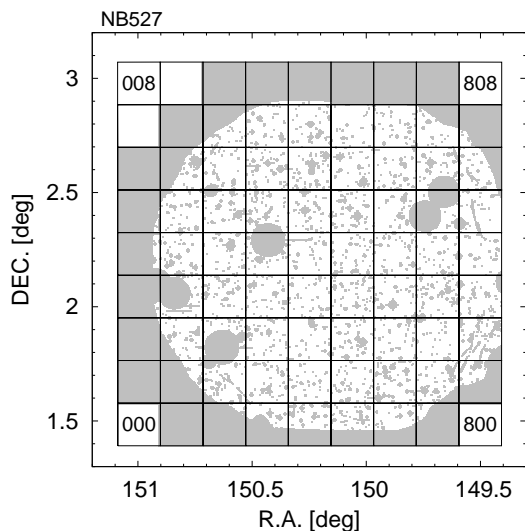


Fig. 2. Masked area (gray shade) in NB527 image as an example. HSC SSP UD COSMOS, tract 9813, is divided into 9×9 patches as indicated by lattice. patch numbers are indicated at four corners.

in the zero-point of NB387 of the SSP PDR2 release (Aihara et al. 2019). This is due to the metallicity effect of the 4,000 Å break in stellar spectra on $NB387 - g$ color. `hscPipe` uses the Pickles spectral templates based on Solar metallicity stars (Pickles 1998) for zero-point estimations. However, the actual stars used for the calibration seem to be dominated by metal-poor halo stars because these stars are faint ($g \sim 20$) and the HSC survey fields are located in high Galactic latitudes. This template mismatch causes a systematic offset of the zero-point only for NB387. A complete description and full analyses are found in appendix of Liang et al. (2020). We did not correct the NB387 magnitudes in the CHORUS PDR1 catalog but recommend users to apply a 0.45 mag subtraction correction to the NB387 magnitudes in the catalog, as recommended by the HSC SSP team.⁹

4 Imaging data quality

4.1 Definition of masked areas

We defined the masked areas in each CHORUS NB image based on the flags from `hscPipe` and the visual inspection conducted by one of the authors. Fig. 2 shows the masked area of the NB527 image as an example. Pixels in each image that satisfied the following conditions of the `hscPipe` flags were selected as masked pixels: `pixelflags_bright_object` is True (pixels affected by bright objects) or `pixelflags_saturatedcenter` is True (pixels affected by count saturation). In addition to these pixels, we also masked the pixels affected by the halos of

bright stars out. Generally, these halos are more prominent in NB images than in BB images probably owing to the multilayer interferometric thin film coating of NBs. We supplementary set larger circular (sometimes elliptical) masks to cover these bright stars' halos if the pixels with the above flags do not cover sufficiently large areas. One of the authors (S.Y.) selected these pixels by eyes. The edge of the FoV was also defined by eyes by the same author to avoid lower S/N regions. The effective survey area of each NB was calculated from the total number of non masked pixels in the image and is listed in Table 2. The exact positions of the masked pixels are available as image files in a FITS format.

4.2 Sizes of point spread functions

We measured a representative FWHM of the PSF in each patch of the CHORUS NB images using `SExtractor`¹⁰ ver 2.19.5 (Bertin & Arnouts 1996). We adopted a median of the `FWHM_IMAGE` measured by `SExtractor` for stellar-like objects, which were not in the masked areas, as the representative FWHM of the PSF. Stellar-like objects were selected depending on the measurements of `SExtractor` as those satisfying the following three criteria: (1) `MAG_AUTO` in a range of [18.0, 22.0] for NB387 and NB527, [18.0, 21.0] for NB718 and NB973, and [19.0, 21.0] for IB945, (2) `ELONGATION` < 1.2 (i.e., nearly circular shape), and (3) `FLAG` < 4 (i.e., not located in a bad position, such as saturated or truncated pixels; see Bertin & Arnouts 1996 for the details). If there were insufficient number of stellar-like objects in a patch because of an extremely small non masked area, we did not measure the FWHM of the PSF. The measured FWHMs and their spatial variations are shown in Fig. 3, and the values of the area-weighted average and the central patch, 404, are listed in Table 2. The FWHM values range from 1'' to 0.6'', depending on the band. The spatial variation in the FWHM values in each NB is as small as < 0.02'', demonstrating the excellent stability of the image quality across the entire FoV of the HSC.

4.3 Limiting magnitudes

We measured the limiting magnitudes in each patch of the CHORUS NB images by conducting aperture photometry at random sky positions with Python packages, `Astropy`¹¹/`photutils`¹². A large number of random positions (10,000 as default, and 5,000 or 1,000 at the edge of the FoV depending on the available area) were prepared in each patch by avoiding the masked pixels and the pixels of the objects detected by `SExtractor` in advance. If the non masked area in a patch was less than 1 arcmin², we did not measure the lim-

flux density calculated from the limiting magnitudes in the next section.

⁹ <https://hsc-release.mtk.nao.ac.jp/doc/index.php/known-problems-2/#hsc-link-10>

¹⁰ <http://www.astromatic.net/software/sextractor>

¹¹ <https://www.astropy.org/>

¹² <https://photutils.readthedocs.io/en/stable/>

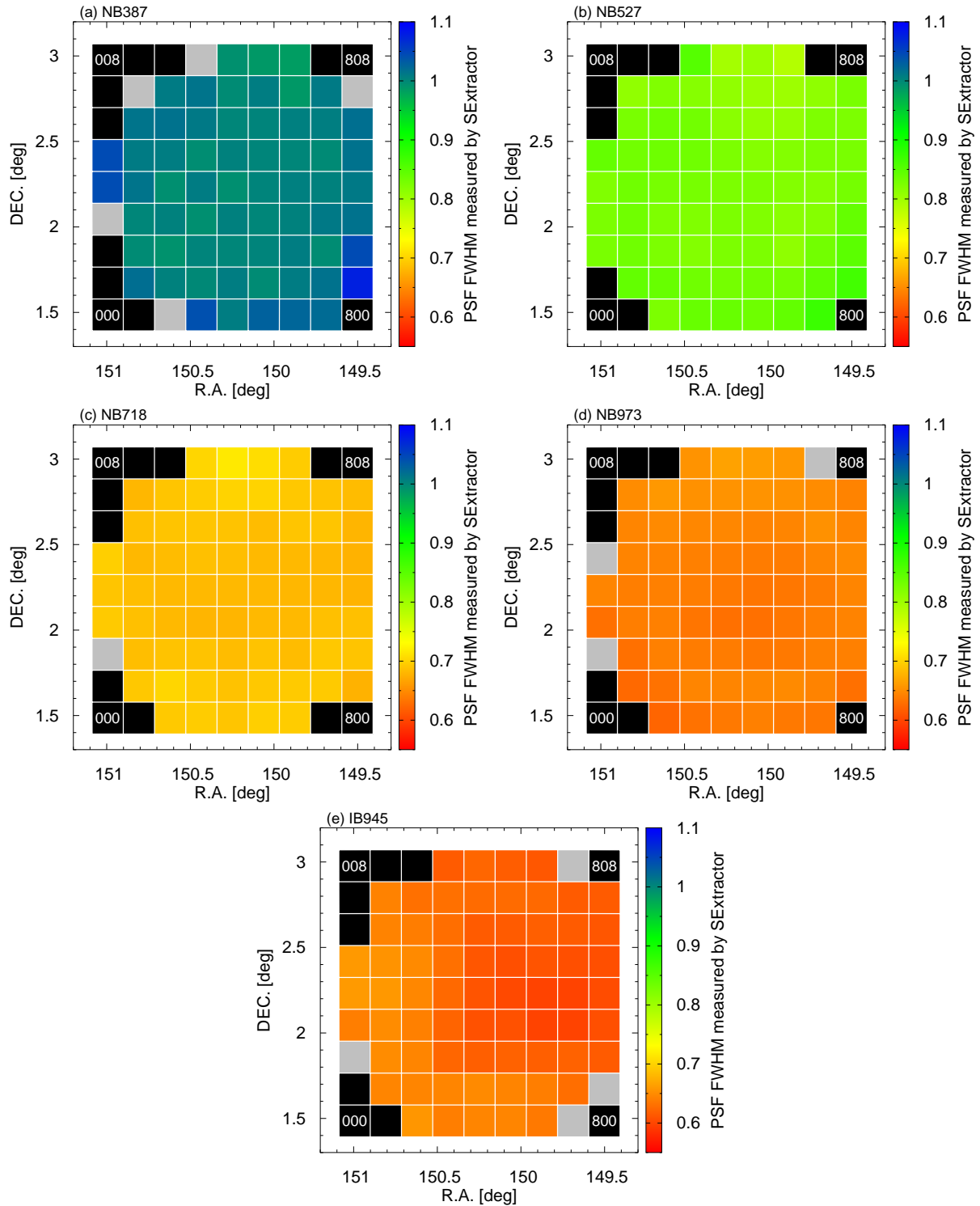


Fig. 3. FWHMs of PSF and their spatial variation for NB387 (top left), NB527 (top right), NB718 (middle left), NB973 (middle right), and IB945 (bottom). Black areas indicate patches that have no effective area. Grey areas indicate patches where there are insufficient number of stars for PSF FWHM measurement owing to small effective area.

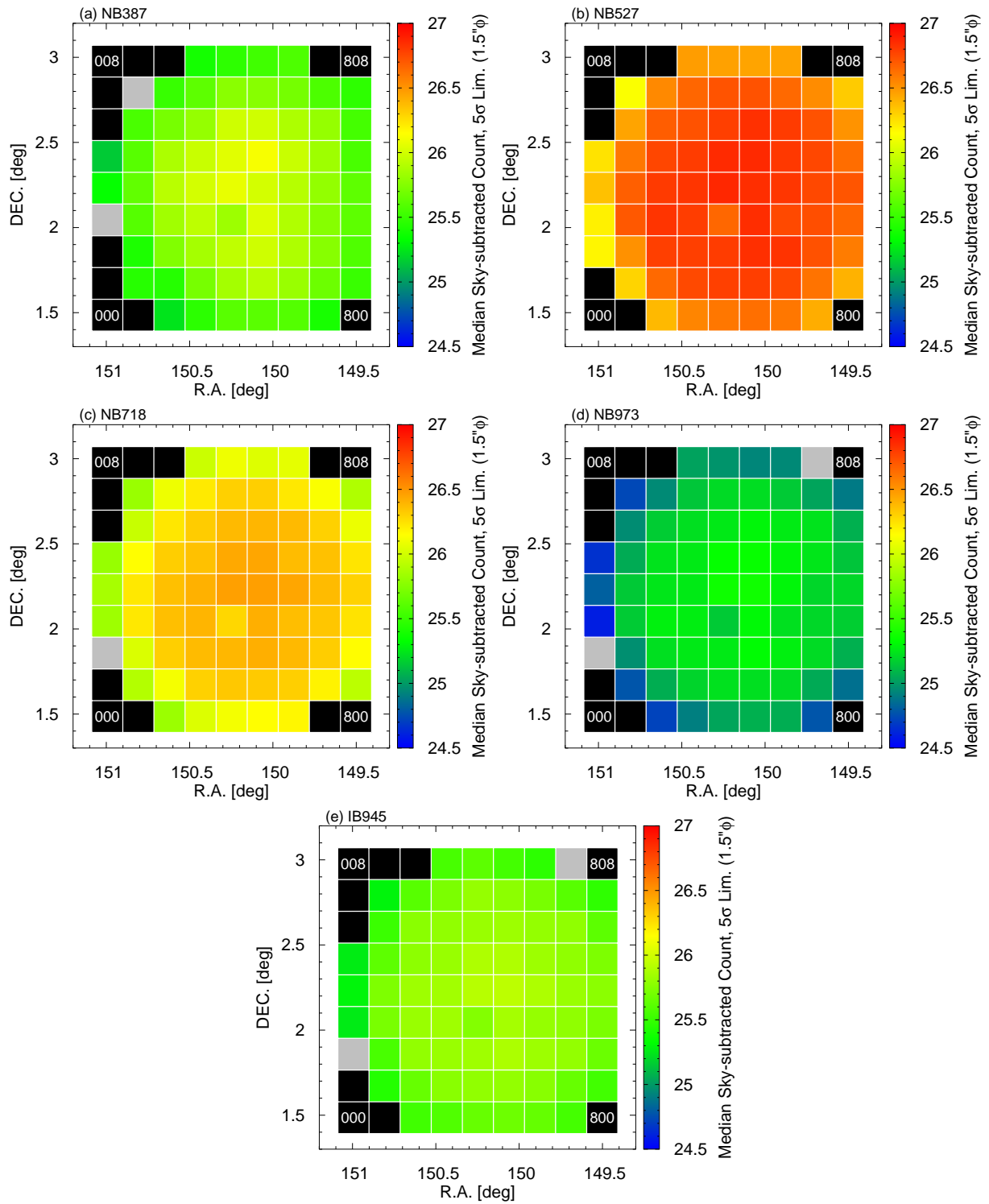


Fig. 4. Five- σ limiting magnitudes and their spatial variation for NB387 (top left), NB527 (top right), NB718 (middle left), NB973 (middle right), and IB945 (bottom). Black areas indicate patches that have no effective area. Grey areas indicate patches where there are insufficient non-masked pixels for limiting magnitude measurements. Aperture size is 1.5'' in diameter.

iting magnitudes. For convenience, we measured the limiting magnitudes with two aperture sizes (1.5'' and 2.0'' in diameter) in each patch of each CHORUS NB image. We estimated the background brightness locally by adopting a median count in an annulus of 1.5'' (2.0'') width and 2.5'' (3.0'') inner diameter set around the 1.5'' (2.0'') aperture and subtracted it from the aperture count as a correction for the background contribution. The standard deviation, σ , was obtained from the histogram of the background-subtracted aperture counts by fitting a Gaussian function. Note that we did not apply any aperture correction to the counts. The 5σ values of the area-weighted average and those in the central patch, 404, for the two aperture sizes are listed in Table 2. The spatial variation in the 5σ values for the 1.5''-diameter aperture case are shown in Fig. 4. We can see a radial dependence of the limiting magnitudes; it is ~ 1 mag shallower at the outer edge compared with that at the center. The patch, 403, shows a shallower depth than the radial trend, which was also reported in Hayashi et al. (2020). This is probably because a half of the four channels in a CCD chip (SDO-ID=0.20/DET-ID=33) close to the patch center was unavailable since November-December 2016 (see the CCD information page of HSC on Subaru Telescope website¹³) and the dithering amount was too small to compensate the low-sensitivity area.

4.4 Completeness

We estimated the detection completeness based on a simulation of embedding and recovering numerous mock galaxies in actual CHORUS NB images using `hscPipe`, `Astropy`, and `GALSIM` (Rowe et al. 2015)¹⁴. These mock galaxies were assumed to have an intrinsic brightness profile described by a circular Sersic profile with index $n = 1.5$ and a half-light radius of 1 pix of the HSC images (0.17''). The adopted radius corresponds to 1.4–0.9 physical kpc for $2 < z < 7$ and very consistent with those of typical LBGs/LAEs (Shibuya et al. 2015; Kawamata et al. 2018). When embedding the mock galaxies into each patch image, we convoluted the brightness profile with the PSF of the image. Because the intrinsic sizes of the mock galaxies were very small compared to the PSF size, the embedded profiles were similar to the PSF but slightly extended. The locations to embed the mock galaxies were chosen randomly, not avoiding the actual objects, to consider the cases in which the extended and bright galaxies overlap and hide faint ones. We considered nine intrinsic magnitudes of the mock galaxies in a range of ± 2.0 magnitudes with a 0.5 magnitude step around the 5σ limiting magnitude. The number of the input mock galaxies was 500 for each intrinsic magnitude in each patch of each band. We ran `hscPipe` to detect the mock galaxies and measure the magnitudes. The criteria for successful recovery were detec-

tion within a radius of 0.5'' from the embedded location and a magnitude difference of less than 0.5 magnitude. We adopted the `undeblended_convolvedflux` magnitude (0.84'' FWHM convolution and $\phi 1.5''$ aperture case, except for NB387, where 1.1'' FWHM convolution and $\phi 2.0''$ aperture case is adopted) as the output total magnitude for Fig. 5; however, the results with the `convolvedflux` magnitude were the essentially same. Note that the `undeblended_convolvedflux` and `convolvedflux` magnitudes are aperture-corrected by a PSF model and equivalent to the total magnitude for the point sources. The detection completeness is defined as the ratio of the number of successfully recovered galaxies to that of embedded mock galaxies. The mock galaxies placed in the masked areas were excluded from the analysis in this final step. To moderate the computation time, we conducted this experiment in only 4 patches of 202, 303, 404, and 606, instead of all the 81 patches.

Fig. 5 shows the results of the simulations of the detection completeness. We find that the completeness is $\gtrsim 60\%$ at the 5σ limiting magnitude ($\phi 2.0''$ not aperture-corrected) in each patch, which is reasonable. Even at magnitudes brighter than the limiting magnitudes, the completeness is only 80–95% and does not reach 100% because of the hiding effect by bright objects. For NB527, the completeness is relatively lower than that of other bands. This seems to be caused by the source confusion due to the very deep depth with a moderate PSF size. Indeed, the surface number density of the detected objects in NB527 up to a 5σ limit of 26.46 AB ($\phi 2.0''$) corresponds to an areal fraction of $\sim 13\%$ even if we assume a circular area with a radius equal to the PSF FWHM size ($r = 0.82''$) per object. For NB973, we also present the average completeness over all the patches estimated similarly but independently by Itoh et al. (2018); it is slightly lower than ours but is broadly consistent. Actually, Itoh et al. (2018) used `hscPipe` version 4.0.5, and their 5σ -limiting magnitude in the 1.5''-diameter aperture of 25.0 was 0.4 magnitude shallower than that of this study.

5 Number counts

For the verification of the CHORUS PDR1 catalog, we calculated the source number counts in the CHORUS NBs and compared the results with those reported in the literature. We adopted the `undeblended_convolvedflux` magnitudes (0.84'' FWHM convolution and $\phi 1.5''$ aperture case, except for NB387, where 1.1'' FWHM convolution and $\phi 2.0''$ aperture case is adopted) as the total magnitude of the objects and excluded the objects and area in the masked regions. The total magnitudes for each object were corrected for the Galactic extinction using the values listed in the CHORUS PDR1 catalog which are estimated from Schlegel et al. (1998) dust maps (see also HSC SSP PDR papers Aihara et al. 2018b; Aihara et al. 2019). These extinction magnitudes are small; for

¹³<https://www.naoj.org/Observing/Instruments/HSC/ccd.html>

¹⁴<https://github.com/GalSim-developers/GalSim>

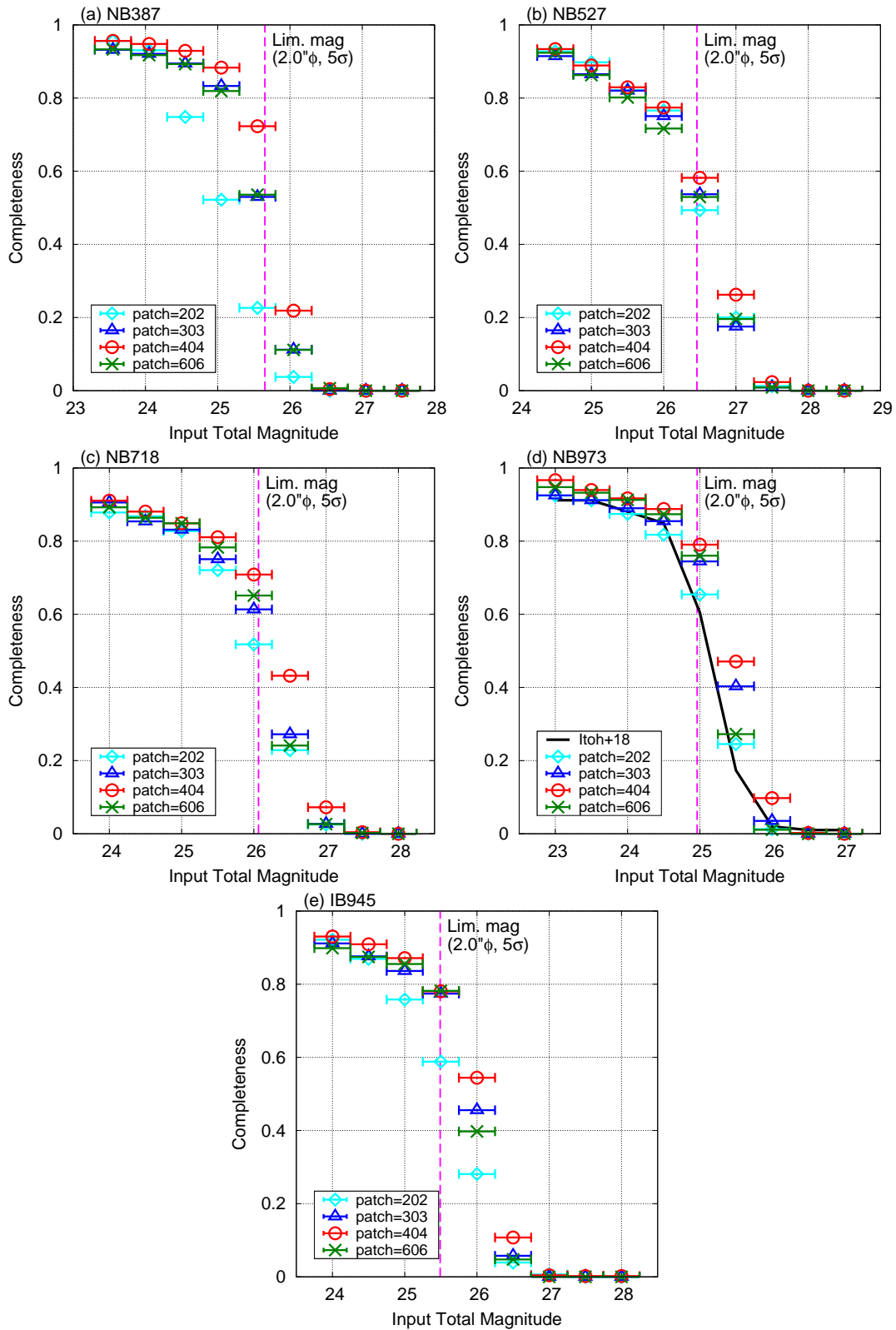


Fig. 5. Detection completeness of NB387 (top left), NB527 (top right), NB718 (middle left), NB973 (middle right), and IB945 (bottom). Cyan, blue, red, and green points with error-bars denote results for patches 202, 303, 404, and 606, respectively. In panel of NB973, black solid line indicates result of Itoh et al. (2018). We also display 5σ limiting magnitudes measured with $2.0''$ -diameter aperture (not total magnitudes) in patch 404 by vertical magenta dashed line in each panel. These results are obtained with `undblended_convolvedflux` magnitudes; however, essentially same results are obtained with `convolvedflux` magnitudes.

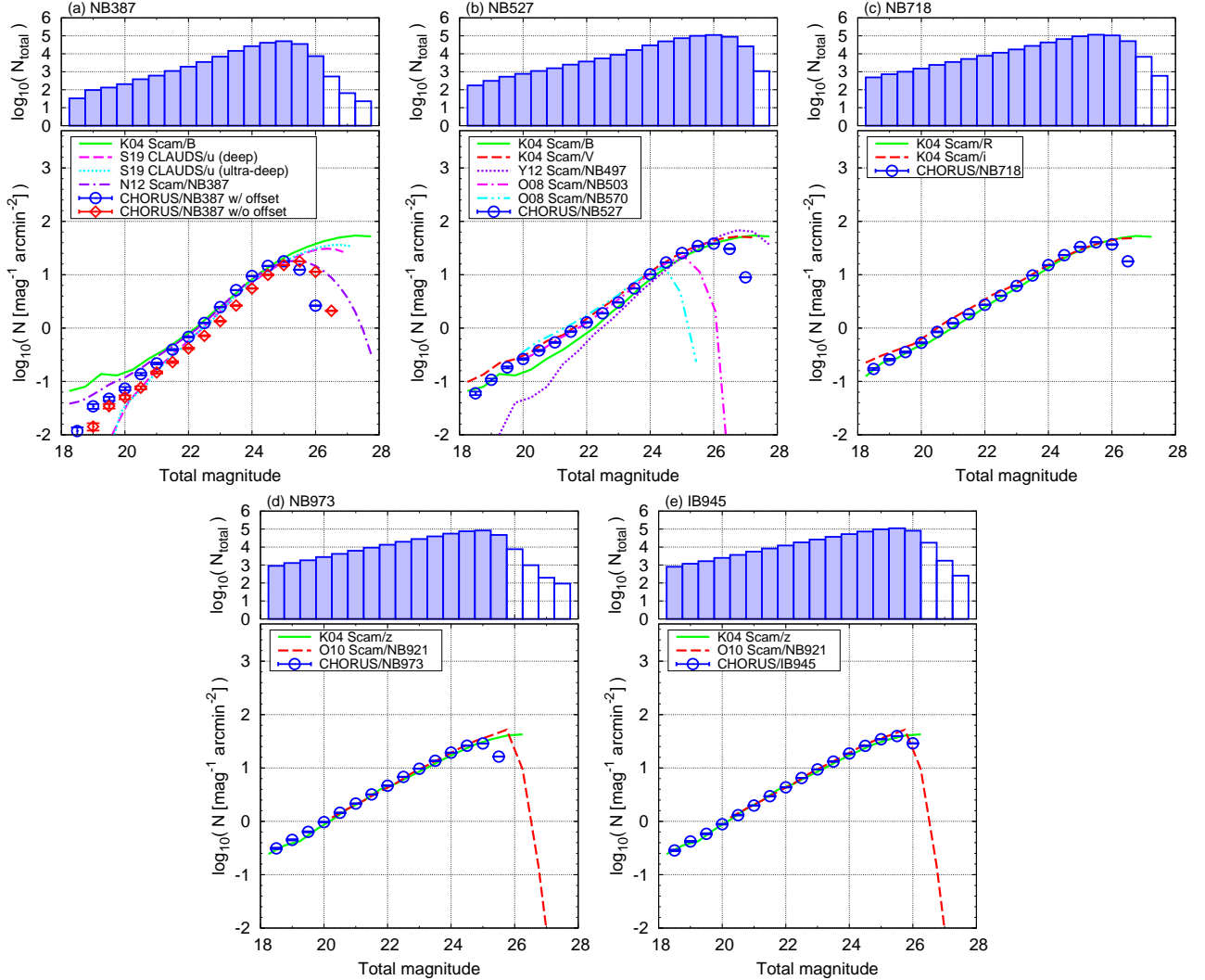


Fig. 6. Source number counts in NB387 (top left), NB527 (top middle), NB718 (top right), NB973 (bottom left) and IB945 (bottom right). For each band, upper panel shows histogram of actual numbers of detected sources and bottom panel shows number density per magnitude per square arcminutes. Empty histogram indicates magnitude range where detection completeness is less than $\sim 10\%$ and probability of spurious detections may be high. Number counts taken from literature are also shown in each panel for comparison. For NB387, we show both number counts with/without zero-point correction for catalog magnitudes produced by `hscPipe` version 6.7. References of literature data: K04: Kashikawa et al. (2004), O08: Ouchi et al. (2008), O10: Ouchi et al. (2010), Y12: Yamada et al. (2012), N12: Nakajima et al. (2012), S19: Sawicki et al. (2019).

instance, ~ 0.1 mag even in NB387 in which the extinction effect is the severest. We also applied a catalog flag, `forced.merge_peak_XXXX` is True, where XXXX = n387, n527, n718, i945, or n973, to ensure that we count only the sources detected in the NB that we are considering. Otherwise, the number count included the sources that were not actually detected in the NB because `hscPipe` lists all the sources detected in any single band in the catalogs. Because the BB images of the HSC SSP are deeper than the CHORUS NB images, numerous faint BB sources, which are not detected in any of the CHORUS NBs, are also listed in the CHORUS PDR1 catalog.

Fig. 6 shows the number count measurements. We only present the data points for those magnitudes at which the completeness (see Fig. 5) is larger than 10%. We also display the literature data of both the BBs and NBs whose wavelengths are close to those of each NB. There are excellent agreements between all the CHORUS number counts and the literature data. For example, the number counts of NB718, NB973, and IB945 present excellent agreement with the data of Subaru/Suprime-Cam (i from Kashikawa et al. 2004 for NB718, and z from Kashikawa et al. 2004 and NB921 from Ouchi et al. 2010 for NB973 and IB945). The NB527 number count also agrees with those of Subaru/Suprime-Cam NB503 from Ouchi et al. (2008) and V from Kashikawa et al. (2004); however, there are slight differences from those in bluer bands, like B from Kashikawa et al. (2004) and NB497 from Yamada et al. (2012). Because the slopes of the number counts reported in the literature are steeper at shorter wavelengths, the CHORUS results seem to follow this trend. For NB387 after the zero-point correction (see sec. 3), the number count data agree with those of Suprime-Cam/NB387 from Nakajima et al. (2012), Suprime-Cam/ B from Kashikawa et al. (2004), and CFHT/MegaCam/ u from Sawicki et al. (2019) at magnitudes fainter than 22. At brighter magnitudes, the NB387 data of ours and Suprime-Cam lie between the two BB literature data, which is reasonable given the trend mentioned above, because the wavelength of NB387 is indeed between those of the B - and u -bands. The zero-point uncorrected NB387 number count is less than those reported in the literature data. These results suggest the necessity and validity of the zero-point correction.

6 How to use the catalog and example use cases of the CHORUS data

The CHORUS PDR1 catalog is available at the Catalog Archive Server (CAS)¹⁵ of the HSC-SSP. An example SQL query to obtain a list of the coordinates, patch, the Galactic extinction in NB387, $\phi 2.0''$ aperture NB387 magnitudes, NB387 total magnitudes (`undeblended_convolvedflux` with $1.1''$ FWHM convolution and $\phi 2.0''$ aperture), and the corresponding aperture

corrections for the sources detected in NB387 is as follows:

```
SELECT
    object_id, ra, dec, patch, a_n387
    n387_undeblended_apertureflux_20_mag
    n387_undeblended_convolvedflux_2_20_mag
    n387_undeblended_convolvedflux_2_20_apcorr
FROM
    s18a_chorus.forced
LEFT JOIN s18a_chorus.forced3 USING
    (object_id)
LEFT JOIN s18a_chorus.forced6 USING
    (object_id)
WHERE
    tractSearch(forced.object_id, 9813)
AND forced.nchild = 0
AND forced.detect_ispatchinner IS True
AND forced.merge_peak_n387 IS True
AND forced.n387_pixelflags_saturatedcenter
    IS False
AND forced.n387_pixelflags_bright_object IS
    False
```

The CHORUS PDR1 (*forced*) catalog consists of 7 files of `s18a_chorus.forced`, `s18a_chorus.forced2`, ..., `s18a_chorus.forced7`. The FITS files of the masked areas (Fig. 2), spatial maps of PSF sizes (Fig. 3) and limiting magnitudes (Fig. 4), numerical data of detection completeness simulations (Fig. 5), and numerical data of measured number counts (Fig. 6) are also available through the website¹⁶.

In the following, we describe four specific studies ongoing with the CHORUS data and other ancillary studies including results published so far.

6.1 Lyman continuum survey of galaxies and AGNs

In the CHORUS project, we are performing a LyC survey for galaxies and AGNs at $z \simeq 3.3$ and 4.9 using NB387 and NB527, respectively (see Fig. 1). The samples are mainly the LAEs selected by NB527 ($z \simeq 3.3$) and NB718 ($z \simeq 4.9$). An average LyC-to-UV flux density ratio, or f_{esc} , of the LAEs will be estimated by stacking analysis. Combining the LyC-to-UV ratios corrected for the IGM transmission and the observed UV luminosity densities, we can estimate the LyC luminosity densities and examine whether galaxies dominate the LyC emissivity at $z \sim 3-5$. We can also detect the LyC from individual LAEs and AGNs. The number of such LyC galaxies at $z > 3$ is still limited (e.g., Iwata et al. 2009; Vanzella et al. 2012; Vanzella et

¹⁵<https://hsc-release.mtk.nao.ac.jp/datasearch/>

¹⁶<https://hsc-release.mtk.nao.ac.jp/doc/index.php/chorus/>

al. 2015; Steidel et al. 2018; Iwata et al. 2019). This program will increase that number significantly. Follow-up spectroscopy of these reliable LyC galaxies allows an f_{esc} calibration from the non-ionizing properties, such as a high [O III]/[O II] ratio (Nakajima & Ouchi 2014; de Barros et al. 2016; Nakajima et al. 2020). Once we establish the relation between the LyC emissivity (or f_{esc}) values and the properties of galaxies observable at longer wavelengths at $z \lesssim 5$, we can estimate f_{esc} of the galaxies in the epoch of reionization ($z > 6$). In this epoch, direct LyC observations are impossible owing to the severe absorption caused by the neutral hydrogen atoms in the IGM (Inoue & Iwata 2008; Inoue et al. 2014).

6.2 Surveys of faint AGNs as dual-emitters

Using NB718 and NB921, we can select a population of faint AGNs at $z \simeq 4.9$ as Ly α -C IV dual emitters if we appropriately treat the effects of broad lines whose line widths are broader than the NB widths (Fig. 1). This selection method is unique because these faint AGNs with a magnitude range similar to that discussed by Giallongo et al. (2015) are difficult to be isolated from the LBGs by any combination of BB colors. Moreover, our NB527 data allows the direct measurement of the LyC of these faint AGNs. The faint-AGN population reported by Giallongo et al. (2015) can reproduce the LyC emissivity required to keep the Universe ionized at $z \sim 5$ –6 if $f_{\text{esc}} = 1$ (Madau & Haardt 2015). We examine if this is the case not only by measuring the faint-AGN LF but also by measuring the f_{esc} of this population. Simultaneously, we measure f_{esc} of galaxies at the same redshift and study their contribution directly. Subsequently, we identify the population that dominates the cosmic LyC emissivity at $z \sim 3$ –5 and infer the source of the cosmic reionization at $z > 6$.

6.3 Surveys of Pop III-dominated galaxies

Pop III stars are expected to have high LyC emissivity and may play a significant role in the early phase of reionization (e.g., Sokasian et al. 2004). However, observational evidence for this stellar population is still inconclusive (e.g., Kashikawa et al. 2012; Rydberg et al. 2015; Vanzella et al. 2020), and its characteristics, e.g., the initial mass function and the LyC emissivity, are unknown. Theoretically, Pop III star clusters can be formed even at $z \sim 2$ –3, depending on the efficiency of the IGM metal-enrichment (e.g., Tornatore et al. 2007; Johnson 2010; de Souza et al. 2011). Indeed, pristine ($Z < 10^{-4}$) gas clouds, from which Pop III stars may form, are found at $z \simeq 3$ (e.g., Fumagalli et al. 2011). Identifying the epoch of the termination of a metal-free star formation is also a very important problem. The He II emission line can be an indicator of Pop III stars (e.g., Tumlinson et al. 2001; Schaerer 2003). Using our well-tuned set of NBs, we can search for Ly α –He II dual emitters at $z \simeq 2.2, 3.3,$ and 4.9

(see Table 1 and Fig. 1). Such a dual emitter search was performed by Nagao et al. (2008) with the Suprime-Cam for $z \sim 4$. We update the upper limit on the He II line luminosity density or the Pop III star formation rate density by Nagao et al. (2008) with a 7 times larger area and up to ~ 1 mag deeper imaging data at a wider redshift range of $z = 2$ –5. This will enable us to constrain the metal-enrichment efficiency in the IGM stronger than before.

6.4 Mapping spatial distributions of ionized bubbles

Because Ly α photons are sensitive to x_{HI} , the distribution of the LAEs depends on both x_{HI} and the large-scale structure (LSS). However, LBGs are selected by the continuum and are not very sensitive to x_{HI} but simply trace the LSS. If we normalize the number density of the LAEs for each location by that of the LBGs, we can isolate the spatial distribution of x_{HI} ; we can visualize the x_{HI} map directly from the LAE-to-LBG density ratio. An essential point is to select LBGs with a similar redshift to the NB-selected LAEs whose redshift variation is as small as $\Delta z \simeq 0.1$. Although such an LBG selection is not feasible by BB filters, we can reach $\Delta z \simeq 0.3$ using an intermediate filter, IB945 for redshifts around $z = 6.6$ and 7.0. From the spatial variation of the observed number density ratio, we can visualize an x_{HI} map far ahead of the future 21 cm experiments, such as the SKA. Such an x_{HI} mapping opens a new pathway to examine the ionization topology, for example, allowing the measurements of the ionized bubble size directly.

6.5 Ancillary sciences

Very wide (1.6 deg^2) and very deep ($\gtrsim 0.1 L_*$) LAE samples at $z \simeq 2.2, 3.3, 4.9, 6.8,$ and 7.0 are obtained by this program. An LAE LF at $z = 7.0$ has already been published as the CHORUS paper II (Itoh et al. 2018) that reports a very similar LF shape to those at $z = 5.7$ and 6.6 with a small overall decrement compared to the lower- z ones. This indicates that the reionization process does not alter the shape of the LAE LF in contrast to a previous claim of a bright-end hump (Zheng et al. 2017). A comprehensive LAE search in the CHORUS data in conjunction with the HSC SSP data is ongoing, adopting a machine learning technique (Ono, Y. et al. in preparation). A study of intensity mapping of Ly α emission is also ongoing (Kikuchihara, S. et al. in preparation). More LAE related studies including environmental ones and optical emission line properties in the near-infrared band are also ongoing. We are also searching for spatially extended LAEs — Ly α blobs — in the imaging data. A result of a Ly α blob survey at $4.9 \leq z \leq 7.0$ has been published recently as the CHORUS paper III (Zhang et al. 2020) that reports a Ly α blob at $z \simeq 7.0$, the highest- z blob found so far. [O II], [O III], H β , and H α emitters at various redshifts are also studied with the CHORUS data in conjunction with the HSC

SSP data (Hayashi et al. 2020) and Spitzer data (Harikane et al. 2018). More line emitter studies including AGN surveys will be performed in future. The CHORUS PDR1 data will be useful for various studies performed all over the world. We strongly encourage the readers' own studies using the dataset.

7 Summary

In this study, we conducted a deep imaging survey using a set of narrow-band (NB) and intermediate-band (IB) filters, named as Cosmic HydrOgen Reionization Unveiled with Subaru (CHORUS), with the Hyper Suprime-Cam (HSC) equipped on the Subaru Telescope. The filter set used in the survey is shown in Figure 1. The wavelengths, NB387, NB527, NB718, NB973, and IB945, summarized in Table 1, were chosen in a very well-organized manner to maximize the scientific outcomes when the filters were used in combination with another NB, NB921, from the Subaru Strategic Program for HSC (HSC SSP). The observations were performed on 18 nights during the period from January 2017 to December 2018 in an intensive program of the Subaru Telescope. The observing field was the COSMOS field (Scoville et al. 2007). The data reduction, source detection, and multiband photometry were conducted using `hscPipe`, the official pipeline software for the HSC developed by the HSC SSP team (Bosch et al. 2018). The `hscPipe` version used was 6.7, the same as that used for HSC SSP public data release (PDR) 2 (Aihara et al. 2019). Because there is a known problem for the `cmode1` magnitudes in this version, we recommended using the `undebledned_convolvedflux` magnitudes instead. The imaging data qualities were examined thoroughly in a spatially dependent manner, as shown in Figures 3 and 4. For each NB/IB, typical values of the size of point spread functions, 5σ limiting magnitude, and survey area excluding the carefully defined masked regions (see Figure 2 as an example) are summarized in Table 2. An extensive set of mock observation simulations was performed to estimate the source detection completeness, as shown in Figure 5. We checked the source number counts and compared them with previous studies in Figure 6. An excellent agreement with the literature data was obtained in each NB/IB. All the images and photometric catalogs are publicly available through the HSC SSP database. This data release is called CHORUS PDR 1.

Acknowledgments

The CHORUS NB/IB filter development was supported by JSPS KAKENHI Grant Numbers 23244033 (KS: NB387), 24244018 (II: NB527), 23244025 (MO: NB921 and NB973), and 23684010 (AKI: IB945), and by a special operating cost grant by MEXT to Ehime University (YT: NB718). This work was also supported by JSPS KAKENHI Grant Numbers 26287034 (AKI, KM), 17H01114 (AKI, KM, SY, MO, II, KS, TN, NK, YO), 15H02064 (MO), and 17H01110 (MO).

The authors would like to thank the referee for constructive comments which were useful to improve the quality of the manuscript. The authors would like to acknowledge their specific contributions by the following people: Ryohei Itoh and Ryota Kakuma for data reduction, Satoshi Kawanomoto and Masakazu A. R. Kobayashi for filter development and inspection, Karin Shimodate for the observations, and Masayuki Tanaka for public data release through the HSC SSP database. The authors would also like to thank the following members of the CHORUS project for their various contributions: Naoki Yasuda, Masayuki Umemura, Masao Mori, Yasuhito Shioya, Toru Yamada, Ikkoh Shimizu, Kenji Hasegawa, Tomoaki Ishiyama, Mana Niida, Akira Konno, Shiro Mukae, Andrea Schulze, Genoveva Micheva, Masayuki Akiyama, Kenichi Tadaki, Michael Strauss, Ryo Higuchi, Takashi Kojima, Masafusa Onoue, Yoshiki Matsuoka, Masatoshi Imanishi, Rhythm Shimakawa, Takuya Hashimoto, Y.-T. Lin, John Silverman, Seiji Fujimoto, Kohei Iwashita, Takuji Yamashita, Tomoko Suzuki, and Hisakazu Uchiyama

The Hyper Suprime-Cam (HSC) collaboration includes the astronomical communities of Japan and Taiwan, and Princeton University. The HSC instrumentation and software were developed by the National Astronomical Observatory of Japan (NAOJ), the Kavli Institute for the Physics and Mathematics of the Universe (Kavli IPMU), the University of Tokyo, the High Energy Accelerator Research Organization (KEK), the Academia Sinica Institute for Astronomy and Astrophysics in Taiwan (ASIAA), and Princeton University. Funding was contributed by the FIRST program from the Japanese Cabinet Office, the Ministry of Education, Culture, Sports, Science and Technology (MEXT), the Japan Society for the Promotion of Science (JSPS), Japan Science and Technology Agency (JST), the Toray Science Foundation, NAOJ, Kavli IPMU, KEK, ASIAA, and Princeton University.

This paper makes use of software developed for the Large Synoptic Survey Telescope. We thank the LSST Project for making their code available as free software at <http://dm.lsst.org>

This paper is based on data collected at the Subaru Telescope and retrieved from the HSC data archive system, which is operated by Subaru Telescope and Astronomy Data Center (ADC) at NAOJ. Data analysis was in part carried out with the cooperation of Center for Computational Astrophysics (CfCA), NAOJ.

The Pan-STARRS1 Surveys (PS1) and the PS1 public science archive have been made possible through contributions by the Institute for Astronomy, the University of Hawaii, the Pan-STARRS Project Office, the Max Planck Society and its participating institutes, the Max Planck Institute for Astronomy, Heidelberg, and the Max Planck Institute for Extraterrestrial Physics, Garching, The Johns Hopkins University, Durham University, the University of Edinburgh, the Queen's University Belfast, the Harvard-Smithsonian Center for Astrophysics, the Las Cumbres Observatory Global Telescope Network Incorporated, the National Central University of Taiwan, the Space Telescope Science Institute, the National Aeronautics and Space Administration under grant No. NNX08AR22G issued through the Planetary Science Division of the NASA Science Mission Directorate, the National Science Foundation grant No. AST-1238877, the University of Maryland, Eotvos Lorand University (ELTE), the Los Alamos National Laboratory, and the Gordon and Betty Moore Foundation.

The authors would like to thank Editage (www.editage.com) for English language editing.

References

- Aihara, H., Arimoto, N., Armstrong, R., Arnouts, S., Bahcall, N. A., Bickerton, S., Bosch, J., Bundy, K., et al. 2018a, PASJ, 70, S4

- Aihara, H., Armstrong, R., Bickerton, S., Bosch, J., Coupon, J., Furusawa, H., Hayashi, Y., Ikeda, H., et al. 2018b, PASJ, 70, S8
- Aihara, H., ALSayyad, Y., Ando, M., Armstrong, R., Bosch, J., Egami, E., Furusawa, H., Furusawa, J., et al. 2019, PASJ, 71, 114
- Bagley, M. B., Scarlata, C., Henry, A., Rafelski, M., Malkan, M., Teplitz, H., Dai, Y. S., Baronchelli, I., et al. 2017, ApJ, 837, 11
- Becker, G. D., Rauch, M., Sargent, W. L. W. 2007, ApJ, 662, 72
- Becker, G. D., Bolton, J. S., Madau, P., Pettini, M., Ryan-Weber, E. V., Venemans, B. P. 2015, MNRAS, 447, 3402
- Bertin, E., & Arnouts, S. 1996, A&AS, 117, 393
- Bianchi, S., Cristiani, S., Kim, T.-S. 2001, A&A, 376, 1
- Bosch, J., Armstrong, R., Bickerton, S., Furusawa, H., Ikeda, H., Koike, M., Lupton, R., Mineo, S., et al. 2018, PASJ, 70, S5
- Carlberg, R. G. 1981, MNRAS, 197, 1021
- Castellano, M., Dayal, P., Pentericci, L., Fontana, A., Hutter, A., Brammer, G., Merlin, E., Grazian, A., et al. 2016, ApJ, 818, L3
- Chambers, K. C., Magnier, E. A., Metcalfe, N., Flewelling, H. A., Huber, M. E., Waters, C. Z., Denneau, L., Draper, P. W., et al. 2016, arXiv:1612.05560
- de Barros, S., Vanzella, E., Amorín, R., Castellano, M., Siana, B., Grazian, A., Suh, H., Balestra, I., et al. 2016, A&A, 585, 51
- de Souza, R. S., Yoshida, N., Ioka, K. 2011, A&A, 533, 32
- Fan, X., Strauss, M. A., Becker, R. H., White, R. L., Gunn, J. E., Knapp, G. R., Richards, G. T., Schneider, D. P., et al. 2006, AJ, 132, 117
- Finkelstein, S. L., D'Aloisio, A., Paardekooper, J.-P., Ryan, R. Jr., Behroozi, P., Finlator, K., Livermore, R., Upton Sanderbeck, P. R., et al. 2019, ApJ, 879, 36
- Fumagalli, M., O'Meara, J. M., Prochaska, J. X. 2011, Science, 334, 1245
- Furusawa, H., Koike, M., Takata, T., Okura, Y., Miyatake, H., Lupton, R. H., Bickerton, S., Price, P. A., et al. 2018, PASJ, 70, S3
- Giallongo, E., Grazian, A., Fiore, F., Fontana, A., Pentericci, L., Vanzella, E., Dickinson, M., Kocevski, D., et al. 2015, A&A, 578, A83
- Grazian, A., Giallongo, E., Boutsia, K., Cristiani, S., Vanzella, E., Scarlata, C., Santini, P., Pentericci, L., et al. 2018, A&A, 613, A44
- Greig, B., & Mesinger, A. 2017, MNRAS, 465, 4838
- Harikane, Y., Ouchi, M., Shibuya, T., Kojima, T., Zhang, H., Itoh, R., Ono, Y., Higuchi, R., et al. 2018, ApJ, 859, 84
- Harikane, Y., Ouchi, M., Ono, Y., Fujimoto, S., Donevski, D., Shibuya, T., Faisst, A. L., Goto, T., et al. 2019, ApJ, 883, 142
- Hasegawa, K., Asaba, S., Ichiki, K., Inoue, A. K., Inoue, S., Ishiyama, T., Shimabukuro, H., Takahashi, K., et al. 2016, arXiv:1603.01961
- Hayashi, M., Shimakawa, R., Tanaka, M., Onodera, M., Koyama, Y., Inoue, A. K., Komiyama, Y., Lee, C.-H., et al. 2020, PASJ, submitted
- Higuchi, R., Ouchi, M., Ono, Y., Shibuya, T., Toshikawa, J., Harikane, Y., Kojima, T., Chiang, Y.-K., et al. 2019, ApJ, 879, 28
- Hu, E. M., Cowie, L. L., Barger, A. J., Capak, P., Kakazu, Y., Trouille, L. 2010, ApJ, 725, 394
- Hu, W., Wang, J., Zheng, Z.-Y., Malhotra, S., Rhoads, J. E., Infante, L., Barrientos, L. F., Yang, H., et al. 2019, ApJ, 886, 90
- Iliev, I. T., Mellema, G., Pen, U.-L., Merz, H., Shapiro, P. R., Alvarez, M. A. 2006, MNRAS, 369, 1625
- Inoue, A. K., Iwata, I., Deharveng, J.-M. 2006, MNRAS, 371, L1
- Inoue, A. K., Iwata, I. 2008, MNRAS, 387, 1681
- Inoue, A. K., Shimizu, I., Iwata, I., Tanaka, M. 2014, MNRAS, 442, 1805
- Inoue, A. K., Hasegawa, K., Ishiyama, T., Yajima, H., Shimizu, I., Umemura, M., Konno, A., Harikane, Y., et al. 2018, PASJ, 70, 55
- Itoh, R., Ouchi, M., Zhang, H., Inoue, A. K., Mawatari, K., Shibuya, T., Harikane, Y., Ono, Y., et al. 2018, ApJ, 867, 46
- Iwata, I., Inoue, A. K., Matsuda, Y., Furusawa, H., Hayashino, T., Kousai, K., Akiyama, M., Yamada, T., Burgarella, D., Deharveng, J.-M. 2009, ApJ, 692, 1287
- Iwata, I., Inoue, A. K., Micheva, G., Matsuda, Y., Yamada, T. 2019, MNRAS, 488, 5671
- Johnson, J. L. 2010, MNRAS, 404, 1425
- Kashikawa, N., Shimasaku, K., Yasuda, N., Ajiki, M., Akiyama, M., Ando, H., Aoki, K., Doi, M., et al. 2004, PASJ, 56, 1011
- Kashikawa, N., Shimasaku, K., Malkan, M. A., Doi, M., Matsuda, Y., Ouchi, M., Taniguchi, Y., Ly, C., et al. 2006, ApJ, 648, 7
- Kashikawa, N., Shimasaku, K., Matsuda, Y., Egami, E., Jiang, L., Nagao, T., Ouchi, M., Malkan, M. A., et al. 2011, ApJ, 734, 119
- Kashikawa, N., Nagao, T., Toshikawa, J., Ishizaki, Y., Egami, E., Hayashi, M., Ly, C., Malkan, M. A., et al. 2012, ApJ, 761, 85
- Kashikawa, N., Ishizaki, Y., Willott, C. J., Onoue, M., Im, M., Furusawa, H., Toshikawa, J., Ishikawa, S., et al. 2015, ApJ, 798, 28
- Kawamata, R., Ishigaki, M., Shimasaku, K., Oguri, M., Ouchi, M., Tanigawa, S. 2018, ApJ, 855, 4
- Kawanomoto, S., Uruguchi, F., Komiyama, Y., Miyazaki, S., Furusawa, H., Finet, F., Hattori, T., Wang, S.-Y., et al. 2018, PASJ, 70, 66
- Komatsu, E., Smith, K. M., Dunkley, J., Bennett, C. L., Gold, B., Hinshaw, G., Jarosik, N., Larson, D., et al. 2011, ApJS, 192, 18
- Komiyama, Y., Obuchi, Y., Nakaya, H., Kamata, Y., Kawanomoto, S., Utsumi, Y., Miyazaki, S., Uruguchi, F., et al. 2018, PASJ, 70, S2
- Konno, A., Ouchi, M., Ono, Y., Shimasaku, K., Shibuya, T., Furusawa, H., Nakajima, K., Naito, Y., et al. 2014, ApJ, 797, 16
- Konno, A., Ouchi, M., Shibuya, T., Ono, Y., Shimasaku, K., Taniguchi, Y., Nagao, T., Kobayashi, M. A. R., et al. 2018, PASJ, 70, 16
- Liang, Y., Kashikawa, N., Cai, Z., Fan, X., Prochaska, J. X., Shimasaku, K., Tanaka, M., Uchiyama, H., et al. 2020, ApJ, in press (arXiv:2008.01733)
- Madau, P., Haardt, F. 2015, ApJ, 813, L8
- Matsuoka, Y., Strauss, M. A., Kashikawa, N., Onoue, M., Iwasawa, K., Tang, J.-J., Lee, C.-H., Imanishi, M., et al. 2018, ApJ, 869, 150
- Matthee, J., Sobral, D., Santos, S., Rottgering, H., Darvish, B., Mobasher, B. 2015, MNRAS, 451, 400
- Micheva, G., Iwata, I., Inoue, A. K., 2017, MNRAS, 465, 302
- Miralda-Escudé, J., Haehnelt, M., Rees, M. J. 2000, ApJ, 530, 1
- Miyazaki, S., Komiyama, Y., Kawanomoto, S., Doi, Y., Furusawa, H., Hamana, T., Hayashi, Y., Ikeda, H., et al. 2018, PASJ, 70, S1
- Nagao, T., Motohara, K., Maiolino, R., Marconi, R., Taniguchi, Y., Aoki, K., Ajiki, M., Shioya, Y. 2005, ApJ, 631, L5
- Nagao, T., Sasaki, S. S., Maiolino, R., Grady, C., Kashikawa, N., Ly, C., Malkan, M. A., Motohara, K., et al. 2008, ApJ, 680, 100
- Nakajima, K., Ouchi, M., Shimasaku, K., Ono, Y., Lee, J. C., Foucaud, S., Ly, C., Dale, D. A., et al. 2012, ApJ, 745, 12
- Nakajima, K., Ouchi, M. 2014, MNRAS, 442, 900
- Nakajima, K., Ellis, R. S., Robertson, B. E., Tang, M., Stark, D. P. 2020, ApJ, 889, 161
- Naidu, R. P., Tacchella, S., Mason, C. A., Bose, S., Oesch, P. A., Conroy, C. 2020, ApJ, in press (arXiv:1907.13130)
- Nakamura, E., Inoue, A. K., Hayashino, T., Horie, M., Kousai, K., Fujii, T., Matsuda, Y. 2011, MNRAS, 412, 2579
- Oke, J. B., 1990, AJ, 99, 1621
- Onoue, M., Kashikawa, N., Willot, C. J., Hiben, P., Im, M., Furusawa, H., Harikane, Y., Imanishi, M., et al. 2017, ApJ, 847, L15
- Ouchi, M., Shimasaku, K., Akiyama, M., Simpson, C., Saito, T., Ueda, Y., Furusawa, H., Sekiguchi, K., et al. 2008, ApJS, 176, 301

- Ouchi, M., Shimasaku, K., Furusawa, H., Saito, T., Yoshida, M., Akiyama, M., Ono, Y., Yamada, T., et al. 2010, *ApJ*, 723, 869
- Ouchi, M., Harikane, Y., Shibuya, T., Shimasaku, K., Taniguchi, Y., Konno, A., Kobayashi, M. A. R., Kajisawa, M., et al. 2018, *PASJ*, 70, S13
- Parsa, S., Dunlop, J. S., McLure, R. J. 2018, *MNRAS*, 474, 2904
- Pickles, A. J., 1998, *PASP*, 110, 863
- Planck collaboration 2018, *A&A*, submitted (arXiv:1807.06209)
- Robertson, B. E., Ellis, R. S., Furlanetto, S. R., Dunlop, J. S. 2015, *ApJ*, 802, L19
- Rowe, B. T. P., Jarvis, M., Mandelbaum, R., et al. 2015, *Astronomy and Computing*, 10, 121
- Rydberg, C.-E., Zackrisson, E., Zitrin, A., Guaita, L., Melinder, J., Asadi, S., Gonzalez, J., Ostlin, G., Ström, T. 2015, *ApJ*, 804, 13
- Santos, S., Sobral, D., Matthee, J. 2016, *MNRAS*, 463, 1678
- Sawicki, M., Arnouts, S., Huang, J., Coupon, J., Golob, A., Gwyn, S., Foucaud, S., Moutard, T., et al. 2019, *MNRAS*, 489, 5202
- Schaerer, D. 2003, *A&A*, 397, 527
- Scoville, N., Aussel, H., Brusa, M., Capak, P., Carollo, C. M., Elvis, M., Giavalisco, M., Guzzo, L., et al. 2007, *ApJS*, 171, 1
- Shibuya, T., Ouchi, M., Harikane, Y. 2015, *ApJS*, 219, 15
- Shibuya, T., Ouchi, M., Konno, A., Higuchi, R., Harikane, Y., Ono, Y., Shimasaku, K., Taniguchi, Y., et al. 2018a, *PASJ*, 70, S14
- Shibuya, T., Ouchi, M., Harikane, Y., Rauch, M., Ono, Y., Mukae, S., Higuchi, R., Kojima, T., et al. 2018b, *PASJ*, 70, S15
- Schlegel, D. J., Finkbeiner, D. P., & Davis, M. 1998, *ApJ*, 500, 525
- Steidel, C. C., Bogosavljević, M., Shapley, A. E., Reddy, N. A., Rudie, G. C., Pettini, M., Trainor, R. F., Strom, A. L. 2018, *ApJ*, 869, 123
- Sokasian, A., Yoshida, N., Abel, T., Hernquist, L., Springel, V. 2004, *MNRAS*, 350, 47
- Taylor, A. J., Barger, A. J., Cowie, L. L., Hu, E. M., Songaila, A. 2020, *ApJ*, in press (arXiv:2004.09510)
- Tilvi, V., Malhotra, S., Rhoads, J. E., Coughlin, A., Zheng, Z., Finkelstein, S. L., Veilleux, S., Mobasher, B., et al. 2020, *ApJ*, 891, L10
- Tornatore, L., Ferrara, A., Schneider, R. 2007, *MNRAS*, 382, 945
- Tumlinson, J., Giroux, M. L., Shull, J. M. 2001, *ApJ*, 550, L1
- Vanzella, E., Guo, Y., Giavalisco, M., Grazian, A., Castellano, M., Cristiani, S., Dickinson, M., Fontana, A., et al. 2012, *ApJ*, 751, 70
- Vanzella, E., de Barros, S., Castellano, M., Grazian, A., Inoue, A. K., Schaefer, D., Guaita, L., Zamorani, G., et al. 2015, *A&A*, 576, 116
- Vanzella, E., Meneghetti, M., Caminha, G. B., Castellano, M., Calura, F., Rosati, P., Grillo, C., Dijkstra, M., et al. 2020, *MNRAS*, 494, L81
- Yamada, T., Nakamura, Y., Matsuda, Y., Hayashino, T., Yamauchi, R., Morimoto, N., Kousai, K., Umemura, M. 2012, *AJ*, 143, 79
- Zhang, H., Ouchi, M., Itoh, R., Shibuya, T., Ono, Y., Harikane, Y., Inoue, A. K., Rauch, M., et al. 2020, *ApJ*, 891, 177
- Zheng, Z.-Y., Wang, J., Rhoads, J., Infante, L., Malhotra, S., Hu, W., Walker, A. R., Jiang, L., et al. 2017, *ApJ*, 842, L22